AIAA SciTech Forum
January 3-7, 2022, San Diego, CA & Virtual
AIAA SCITECH 2022 Forum

10.2514/6.2022-0735

Real-Gas Effects on Hypersonic Boundary-Layer Receptivity to Freestream Acoustic Disturbances

Anand R. Varma* and Xiaolin Zhong†
University of California, Los Angeles, California, 90095, USA

In high-enthalpy hypersonic flows, temperatures can be high enough to induce significant real-gas effects, such as finite-rate chemistry and vibrational excitation. While there has been a considerable amount of research on real-gas effects on hypersonic boundary-layer stability, its impact on boundary-layer receptivity to freestream disturbances is not as well understood. This work presents the results of an ongoing Direct Numerical Simulation (DNS) and Linear Stability Theory (LST) study on real-gas effects on the receptivity of a Mach 5 axisymmetric cone boundary layer to freestream planar acoustic disturbances, modeled as Gaussian pulses. In order to parameterize real-gas effects, two cases with different gas models are considered. The first case uses a 5-species, two-temperature thermochemical nonequilibrium (TCNE) gas model, whereas the second case uses a chemically and vibrationally frozen gas model. LST results indicated that real-gas effects are destabilizing to the second mode, leading to longer instability regions, larger growth rates, and a larger N-factor envelope. Unsteady DNS results indicated that real-gas effects do not change the fundamental receptivity mechanism, in that the streamwise behavior of the boundary-layer disturbance induced by the freestream disturbance is qualitatively similar in both phase speed and growth rate between the two gas models. However, real-gas effects led to larger boundary-layer disturbance amplitudes after second-mode growth. In contrast, the receptivity coefficients of the second mode itself were smaller in the real-gas case, indicating that real-gas effects can have competing impacts on second-mode receptivity versus second-mode growth.

I. Introduction

Hypersonic flight continues to see considerable amounts of research due to its potential to yield significant advances in defense, commercial air travel, and space exploration. However, the extreme temperatures encountered in this flight regime still pose a substantial challenge for hypersonic vehicle design. In many cases, a thermal protection system (TPS) is necessary to protect the underlying structure of the vehicle from excessive heating. Unfortunately, the use of a TPS may also hinder the feasibility of a hypersonic vehicle, in terms of both aerodynamic performance and cost. An alternate solution to the heating problem is to modify the behavior of the boundary layer on the surface of the vehicle. Because laminar flows are far less efficient in terms of heat transfer than turbulent flows, it is possible to reduce overall heating to the vehicle by delaying laminar-to-turbulent transition.

In a hypersonic boundary layer, laminar-to-turbulent transition typically occurs due to the presence of environmental disturbances, such as freestream perturbations or surface roughness. Commonly, these environmental disturbances are weak, in which case transition occurs through a four-stage process of receptivity, linear growth, nonlinear breakdown, and finally transition itself. In the receptivity stage, the environmental disturbances generate and excite boundary-layer disturbances. In the linear growth phase, these initially small boundary-layer disturbances then undergo amplification due to boundary-layer instabilities. The dominant boundary-layer instability for slender cones at zero angle-of-attack in the hypersonic regime is Mack's[1] second mode, an acoustic-like instability that is destabilized with increasing freestream Mach number. Once the amplitude of the boundary-layer disturbance becomes large enough, it enters the nonlinear breakdown

*Ph.D. Student, Mechanical and Aerospace Engineering, varmaar@ucla.edu, AIAA Student Member.
†Professor, Mechanical and Aerospace Engineering, xiaolin@seas.ucla.edu, AIAA Associate Fellow.

phase, whereby nonlinear processes (such as resonance between modes) become significant, eventually leading to transition.

In order to accurately predict transition location, it is necessary to not only determine the growth rates of the boundary-layer disturbance in the linear and nonlinear phases, but also the initial amplitude of the boundary-layer disturbance, which is determined by the receptivity process. While it is possible to predict growth rates in the linear growth phase theoretically through linear stability theory (LST), separate receptivity analyses using data from direct numerical simulations (DNS) or experiments are necessary to obtain the initial amplitude of the second-mode disturbance.

High temperatures in high-enthalpy hypersonic flows can induce real-gas effects, such as chemistry (species dissociation and recombination) and vibrational excitation. However, both of these processes occur at a finite rate. Because of the extreme velocities in a hypersonic flow, the flowfield can have drastically different properties depending on the ratio of the characteristic flow timescale (τ_f), called the residence time, to the timescale of finite-rate chemistry (τ_c) or vibrational excitation (τ_v). If $\tau_f \gg \tau_c, \tau_v$, the flow is effectively in thermochemical equilibrium; the chemical composition changes instantaneously with the local thermodynamic state and all internal energy modes (translation, rotation, vibration, etc.) are in equilibrium with one another. If $\tau_f \ll \tau_c, \tau_v$, the chemical composition and vibrational energy will effectively remain frozen throughout the flowfield, since the fluid is advected away before finite-rate chemistry or vibrational excitation can occur. In many cases, $\tau_f \sim \tau_c, \tau_v$, and the flow is said to be in thermochemical nonequilibrium (TCNE). Here the thermochemical state of the fluid is determined not only by the local thermodynamic properties, but also by the advection of the fluid itself. There can also be cases in which flows are simultaneously in thermal equilibrium and chemical nonequilibrium, but the discussion above still stands.

The additional complexity of a thermochemical nonequilibrium gas model has meant that most numerical studies of hypersonic boundary-layer flows have used a perfect gas model. This is justified on the grounds that it remains valid for many scenarios. For example, the perfect gas model is a good approximation for the low-enthalpy, "cold" flows encountered in many ground test facilities. However, it may not be valid for high-enthalpy, "hot" flows, such as those found in high-enthalpy shock tunnels and certain flight conditions (such as the Mach 20 Re-entry F experiment). In such cases, it is necessary to account for real-gas effects in order to accurately predict boundary-layer transition location.

The question as to whether real-gas effects are stabilizing or destabilizing to second-mode growth depends on the nature of the energy exchange involved. The studies of Malik,[2] Chang *et al.*,[3] Stuckert and Reed,[4] Johnson *et al.*,[5] Hudson *et al.*[6] and Mortensen[7] have found that in general, endothermic reactions (like dissociation) are stabilizing to the second mode whereas exothermic reactions (like recombination) are destabilizing. Knisely and Zhong[8] have found that vibrational nonequilibrium has a destabilizing effect on the second mode compared to a frozen flow if the vibrational temperature lags behind the translation-rotation temperature ($T_v < T$). In addition, they found that the supersonic mode was particularly sensitive to vibrational nonequilibrium effects.

In comparison, fewer studies have considered real-gas effects on receptivity itself. Ma and Zhong[9,10] studied real-gas effects on boundary-layer receptivity for Mach 10 oxygen flow over a flat plate. They found that after imposing acoustic waves to the freestream, the wall-response coefficient (the amplitude of the second mode at the branch II neutral point) was considerably larger for a real-gas flow compared to a perfect gas flow. Parsons and Zhong[11] studied the receptivity of a Mach 15 blunt-cone flow to a freestream planar fast acoustic disturbances. Compared to a perfect gas flow, they found that real-gas effects led to greater disturbance amplitudes, although they did not observe any second-mode instabilities. Prakash[12] studied the receptivity of a Mach 5.71 flow over a blunt cone to a planar fast acoustic disturbance and found that the resulting boundary-layer disturbance amplitudes were similar between real-gas and ideal gas models.

The relative lack of studies has meant that the current understanding of real-gas effects on receptivity is limited. Real-gas effects could have completely different impacts on receptivity for different Mach numbers, wall temperatures, geometries, and so on. However, the existing research is limited to a very small number of cases. There is also no data on real-gas effects on second-mode receptivity coefficients for any freestream disturbance. The objective of the present study is to expand on the existing knowledge base by considering real-gas effects on second-mode receptivity for a Mach 5 cold-wall axisymmetric cone boundary layer to both fast and slow acoustic disturbances.

II. Simulation Conditions

The freestream conditions used in this study are presented in Table 1. These conditions are taken from Knisely and Zhong[13] and are intended to resemble conditions found at the Caltech T5 Hypervelocity Shock Tunnel. In order to parameterize real-gas effects, two cases with two different gas models are considered for the same freestream conditions. The first case uses a thermochemical nonequilibrium (TCNE) 5-species air model, hereafter referred to as the real-gas case, whereas the second uses a chemically and vibrationally frozen gas model where the species mass fractions and vibration temperatures are held at their freestream values. In the real-gas case, the wall is isothermal at 300 K for the translation-rotation (T-R) temperature with thermal equilibrium for the vibration temperature and a supercatalytic condition for the species mass fractions. In the frozen gas case, the wall is isothermal at 300 K for the T-R temperature, with the vibration temperature and species mass fractions set to their freestream values.

Table 1. Freestream conditions for DNS simulations.

Parameter	Value	Parameter	Value
M_∞	5	$H_{0,\infty}$	9.17 MJ/kg
ρ_∞	2.322 $\times 10^{-2}$ kg/m^3	p_∞	10 kPa
T_∞	1491.3 K	U_∞	3882.42 m/s
Re_1	1.72 $\times 10^6$ m^{-1}	α	0°
Y_{N_2}	0.78	Y_{O_2}	0.22

The geometry is a circular cone with nose radius $r_n = 1$ mm and a half-angle of 5°. The physical domain is 1 meter in length from nosetip to base. The computational grid uses 512 points in the wall-normal direction, whereas the streamwise grid resolution varies between 100 points per millimeter near the nose to 5 points per millimeter on the frustum.

III. Governing Equations and Gas Model

The governing equations in this study are the same as those used by Mortensen and Zhong.[14–19] Their formulation is summarized here for clarity. The equations are formulated for thermochemical nonequilibrium with a five species air model (N_2, O_2, NO, N and O) to simulate chemistry and a two-temperature model to simulate vibrational nonequilibrium. The rotational mode is assumed to be fully excited and in equilibrium with the translation mode. Two temperatures are used to represent translation-rotation energy and vibration energy, respectively. The Navier-Stokes equations in conservation form consist of five species mass conservation equations, three momentum conservation equations, the total energy equation, and the vibration energy equation. The governing equations in vector form are written as

$$\frac{\partial U}{\partial t} + \frac{\partial F_j}{\partial x_j} + \frac{\partial G_j}{\partial x_j} = W \tag{1}$$

where U is the state vector of conserved quantities and W is the source terms, and F_j and G_j are the inviscid and viscous flux vectors respectively.

$$U = \begin{bmatrix} \rho_1 \\ \vdots \\ \rho_{ns} \\ \rho u_1 \\ \rho u_2 \\ \rho u_3 \\ \rho e \\ \rho e_v \end{bmatrix}, \quad W = \begin{bmatrix} \omega_1 \\ \vdots \\ \omega_{ns} \\ 0 \\ 0 \\ 0 \\ 0 \\ \sum_{s=1}^{nms} \left(Q_{T-V,s} + \omega_s e_{v,s} \right) \end{bmatrix}.$$

The inviscid and viscous flux vectors, F_j and G_j, respectively, are defined by

$$F_j = \begin{bmatrix} \rho_1 u_j \\ \vdots \\ \rho_{ns} u_j \\ \rho u_1 u_j + p\delta_{1j} \\ \rho u_2 u_j + p\delta_{2j} \\ \rho u_3 u_j + p\delta_{3j} \\ (p + \rho e)\, u_j \\ \rho e_v u_j \end{bmatrix}$$

$$G_j = \begin{bmatrix} \rho_1 v_{1j} \\ \vdots \\ \rho_{ns} v_{nsj} \\ \tau_{1j} \\ \tau_{2j} \\ \tau_{3j} \\ -u_i\tau_{ij} - k_T \frac{\partial T}{\partial x_j} - k_V \frac{\partial T_V}{\partial x_j} + \sum_{s=1}^{nms} \rho_s h_s v_{sj} \\ -k_V \frac{\partial T_V}{\partial x_j} + \sum_{s=1}^{nms} \rho_s e_{v,s} v_{sj} \end{bmatrix}$$

where v_{sj} is the species diffusion velocity, and

$$\tau_{ij} = \mu \left(\frac{\partial u_i}{\partial x_j} + \frac{\partial u_j}{\partial x_i} \right) - \frac{2}{3} \mu \frac{\partial u_k}{\partial x_k} \delta_{ij} \tag{2}$$

is the viscous stress. The total energy per unit volume, ρe, is defined as

$$\rho e = \sum_{s=1}^{ns} \rho_s c_{v,s} T + \rho e_v + \frac{1}{2} \rho \left(u_1^2 + u_2^2 + u_3^2 \right) + \sum_{s=1}^{ns} \rho_s h_s^o \tag{3}$$

where h_s^o is the species heat of formation, $e_{v,s}$ is the species specific vibration energy, and $c_{v,s}$ is the species translation-rotation specific heat at constant volume, defined as

$$c_{v,s} = \begin{cases} \frac{5}{2} \frac{R}{M_s} & s = 1, 2, \ldots, nms \\ \frac{3}{2} \frac{R}{M_s} & s = nms + 1, \ldots, ns. \end{cases} \tag{4}$$

The vibration energy per unit volume, ρe_v, is defined as

$$\rho e_v = \sum_{s=1}^{nms} \rho_s e_{v,s} = \sum_{s=1}^{nms} \rho_s \frac{R}{M_s} \frac{\theta_{v,s}}{\exp\left(\theta_{v,s}/T_V\right) - 1} \tag{5}$$

where $\theta_{v,s}$ is the characteristic vibrational temperature of each vibrational mode. The characteristic vibration temperatures are taken from Park.[20] To model chemical nonequilibrium, three dissociation reactions and three exchange reactions are used. Each reaction is governed by a forward and backward reaction rate determined from

$$k_f = C_f T_a^{\eta} \exp\left(-\theta_d / T_a\right) \tag{6}$$

$$k_b = k_f / K_{eq} \tag{7}$$

where all forward reaction rates are obtained from Park.[20] The equilibrium coefficient, K_{eq}, is determined using

$$K_{eq} = A_0 \exp\left(\frac{A_1}{Z} + A_2 + A_3 \ln(Z) + A_4 Z + A_5 Z^2 \right), \tag{8}$$

$$Z = \frac{10000}{T} \tag{9}$$

which is a curve fit to experimental data from Park.[20]

The source term in the vibration energy equation representing the energy exchange between the translation-rotation and vibration modes is calculated using the Landau-Teller formulation:

$$Q_{T-V,s} = \rho_s \frac{e_{v,s}(T) - e_{v,s}(T_V)}{<\tau_s> + \tau_{cs}} \tag{10}$$

where $<\tau_s>$ is the Landau-Teller relaxation time given by Lee.[21] The term τ_{cs} from Park[20] is used to more accurately model the relaxation time in areas of high temperatures occurring just downstream of the bow shock.

The viscosity of each species is computed using a Blottner curve fit, with coefficients from Blottner *et al.*[22] The mixture viscosity and thermal conductivities for each energy mode are found using Wilke's[23] mixing rule. The diffusion velocity is computed using Fick's law assuming a constant Schmidt number of 0.5.

IV. Numerical Methods

A. Direct Numerical Simulation (DNS)

This work uses the thermochemical nonequilibrium shock-fitting code developed by Mortensen and Zhong.[14–19] Their formulation is summarized here for clarity. Since for shock-fitting computations the shock location is not known *a priori*, its position is solved along with the flow field. Accordingly, the computational grid is also a function of time. This leads to the coordinate transformation of the governing conservation equations,

$$\frac{1}{J}\frac{\partial U}{\partial \tau} + \frac{\partial E'}{\partial \xi} + \frac{\partial F'}{\partial \eta} + \frac{\partial G'}{\partial \zeta} + \frac{\partial E'_v}{\partial \xi} + \frac{\partial F'_v}{\partial \eta} + \frac{\partial G'_v}{\partial \zeta} + U\frac{\partial (1/J)}{\partial \tau} = \frac{W}{J} \tag{11}$$

where J is the Jacobian of the coordinate transformation. More details about this transformation can be found in the work of Mortensen.[19] The seven-point finite-difference stencil of Zhong[24] is used to discretize the spatial derivatives,

$$\frac{\partial f_i}{\partial x} = \frac{1}{h b_i} \sum_{k=-3}^{3} \alpha_{i+k} f_{i+k} - \frac{\alpha}{6! b_i} h^5 \left(\frac{\partial f^6}{\partial^6 x} \right) \tag{12}$$

where h is the step size. Setting $\alpha < 0$ yields a fifth order upwind explicit scheme, whereas $\alpha = 0$ reduces to a sixth order central scheme. The inviscid terms use $\alpha = -6$ which yields a low dissipation fifth order upwinded difference and the viscous terms use $\alpha = 0$. Derivatives in the azimuthal direction are computed through Fourier collocation. Second derivatives are computed by applying the first order derivative operator twice. Flux splitting is used for the inviscid flux terms, where the eigenvalues of Λ have been derived for thermochemical nonequilibrium by Liu and Vinokur.[25]

The shock is assumed to be infinitely thin, such that the chemical composition and vibration temperature remain constant across the shock. A complete derivation of the thermochemical nonequilibrium shock fitting procedure can be found in the work of Mortensen.[19] The 3rd-order Runge-Kutta method of Shu and Osher[26] and the forward Euler method are used to advance the solution in time, depending on accuracy and stability requirements. It should be noted that for the real-gas case in this study, the low wall temperature led to excessively stiff chemical reactions near the wall. To resolve this, the approach of Scalabrin[27] is used, whereby the forward and backward reaction rates are computed using a modified temperature

$$T'_f = \frac{1}{2}\left((T_f + T_{min}) + \sqrt{(T_f - T_{min})^2 + \epsilon^2} \right) \tag{13}$$

where $T_{min} = 450$ K and $\epsilon = 0$ K in this work. T_f can be the T-R temperature or the vibration temperature. Lastly, the frozen flow is simulated by setting all source terms $W = 0$ in Equation 1 and forcing the vibration temperatures and species mass fractions to their freestream values.

B. Linear Stability Theory (LST)

This work uses the linear stability theory (LST) code of Mortensen,[19] which has since been expanded upon by Knisely and Zhong.[13] This code partially relaxes the parallel meanflow assumption in that a nonzero meanflow wall-normal velocity can be used. In addition, the shock boundary conditions developed by Knisely and Zhong[13] have been implemented.

The LST equations are derived from the Navier-Stokes equations by a perturbation expansion of the form $q = \overline{q} + q'$, where q is some flow quantity, $\overline{q}$ is the meanflow quantity, and q' is the perturbation quantity. The steady flow terms can be subtracted out, since they satisfy the governing equations themselves. The perturbation quantities are assumed to be small such that higher order terms can be ignored. The meanflow is assumed to be parallel, i.e. $\overline{q} = \overline{q}(y)$. This is an appropriate assumption, since gradients in the wall-normal direction are usually much greater than gradients in the streamwise direction. The perturbation terms are then assumed to take the form of a normal mode such that $q' = \hat{q}(y) \exp\left[i\left(\alpha x + \beta z - \omega t\right)\right]$, where ω is the circular frequency of the disturbance and α and β are the wave numbers in the streamwise and spanwise directions respectively. This study is concerned with spatial stability, where ω is real and specified as a parameter. In addition, α is complex and can be written as $\alpha = \alpha_r + i\alpha_i$. Here, α_r is the streamwise wave number and $-\alpha_i$ is the growth rate. A positive value for $-\alpha_i$ corresponds to growth, whereas a negative value of $-\alpha_i$ corresponds to decay. Substituting the normal mode form of the perturbation quantities into the governing equations then yields a set of $ns + 5$ coupled ordinary differential equations of the form

$$\left(\mathbf{A}\frac{d^2}{dy^2} + \mathbf{B}\frac{d}{dy} + \mathbf{C}\right)\vec{\phi} = \vec{0}. \tag{14}$$

where $\vec{\phi} = \left[\hat{\rho}_1, \hat{\rho}_2, \ldots, \hat{\rho}_{ns}, \hat{u}, \hat{v}, \hat{w}, \hat{T}, \hat{T}_V\right]^T$, $\mathbf{A}$, $\mathbf{B}$ and $\mathbf{C}$ are complex square matrices of size $ns + 5$, and ns is the number of species in the gas model. Further details regarding the derivation of these matrices can be found in the work of Knisely.[28]

The wall boundary conditions for the perturbation quantities are non-catalytic for species densities, no slip for velocity, and zero perturbation for both temperatures. The freestream boundary conditions are the shock boundary conditions of Knisely and Zhong.[13] Frozen LST is performed by setting the source terms, diffusion coefficients, vibrational conductivities, and their derivatives to zero. In addition, the meanflow vibration temperature is set to zero. The perturbation in vibration temperature and species density for all species except N_2 and O_2 is set to zero as well. This is done so that the terms associated with diffusion, vibrational conduction and the vibrational excitation do not affect the perturbation, as is the case for the frozen DNS. In addition, the non-catalytic boundary condition is replaced by a supercatalytic boundary condition, which in this case is essentially equivalent to a perfect gas boundary condition. In both cases, the meanflow wall-normal velocity is assumed to be zero in order to improve convergence. Knisely and Zhong[29] have shown that this assumption has a negligible impact on second-mode phase speeds and growth rates when the supersonic mode is not of concern.

C. Freestream Disturbance Model

The freestream disturbances are modeled using the planar Gaussian pulse model (see Figure 1) of Huang[30] and He and Zhong.[31] The primary advantage in using a pulse disturbance is that its continuous frequency spectrum allows a continuous range of boundary-layer disturbance frequencies to be considered. This can then be used to obtain a spectrum of receptivity coefficients, allowing more insight into the nature of the receptivity process.

In the freestream disturbance model, the disturbances are superimposed onto the steady freestream base flow. The local disturbance at a point (x, y, z) at time t associated with a weak planar Gaussian pulse at zero incidence-angle is

$$\begin{bmatrix} u' \\ v' \\ p' \\ \rho' \end{bmatrix}_\infty = \begin{bmatrix} \Delta u \\ \Delta v \\ \Delta p \\ \Delta \rho \end{bmatrix}_\infty \exp\left(-\frac{R_c^2}{2\sigma^2}\right) \tag{15}$$

where Δ denotes the amplitude of the disturbance, R_c is the distance to the center of the pulse and σ is a

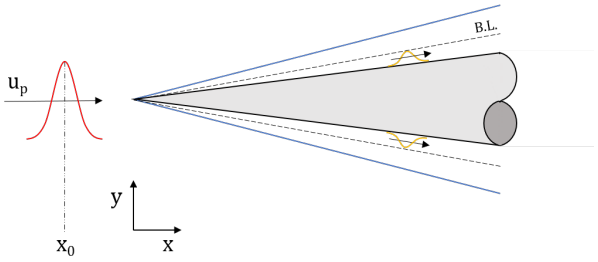

Figure 1. Schematic of a Gaussian pulse disturbance generating boundary-layer disturbances downstream of the bow shock of a blunt cone. Not to scale.

nondimensional quantity which determines both the shape and frequency content of the pulse. Here,

$$R_c = \sqrt{(x - x_c)^2} \tag{16}$$

$$x_c = x_0 + u_p t \tag{17}$$

where x_c is the location of the center of the pulse at time t, x_0 is the initial location of the center of the pulse, and u_p is the pulse velocity. Note that for both the real-gas and frozen cases, the freestream disturbance is assumed to be frozen, allowing it to be specified using only four variables as in Eq. 15. We expect this to be an appropriate assumption, as Knisely and Zhong[8] have found that vibrational effects (which occur at a faster rate than finite-rate chemistry) in the boundary layer are essentially frozen in the perturbation timescale for the relevant second-mode frequencies. Considering that boundary-layer temperatures are higher than in the freestream, the freestream disturbance can be assumed to be frozen as well.

The characteristics of the various types of disturbance (fast acoustic, slow acoustic, etc.) are determined by a dispersion relation. The dispersion relations used in this study are based on the notation of Ma and Zhong.[32–34] For fast and slow acoustic waves at zero incidence angle, the dispersion relations are written as follows:

Fast acoustic wave:

$$\frac{\Delta\rho}{\rho_\infty} = \frac{\Delta p}{\gamma_{t-r} p_\infty} = \frac{\Delta u}{a_\infty} = \epsilon \qquad \Delta v = 0 \tag{18}$$

Slow acoustic wave:

$$\frac{\Delta\rho}{\rho_\infty} = \frac{\Delta p}{\gamma_{t-r} p_\infty} = -\frac{\Delta u}{a_\infty} = \epsilon \qquad \Delta v = 0 \tag{19}$$

where γ_{t-r} is the specific heat ratio associated with the translation-rotation modes and ϵ is a small nondimensional parameter that determines the peak amplitude of the wave. Other variables can be computed through the assumption of a chemically and vibrationally frozen gas. In addition, fast and slow acoustic disturbances propagate at a speed $u_p = u_\infty + a_\infty$ and $u_\infty - a_\infty$ respectively, where a_∞ is the freestream speed of sound.

The freestream pulses in this study use the parameters listed in Table 2. The shape and amplitude spectrum of the pulses for these parameters are shown in Figure 2. The pulse width parameter σ was chosen to excite frequencies up to $f = 1200$ kHz. Note that since the fast acoustic and slow acoustic pulses have different pulse velocities, the pulse width parameter must be scaled differently to yield the same amplitude spectrum. Here, $\sigma = 1 \times 10^{-3}$ was chosen as a baseline value, and was scaled by $1 + 1/M_\infty$ for the fast acoustic pulse and $1 - 1/M_\infty$ for the slow acoustic pulse. Finally, the amplitude ϵ was chosen to yield an approximately linear disturbance.

Table 2. Pulse parameters for receptivity simulations.

Parameter	Fast Acoustic	Slow Acoustic
ϵ	1×10^{-5}	1×10^{-5}
σ	1.2×10^{-3}	0.8×10^{-3}
x_0/r_n	-12	-12

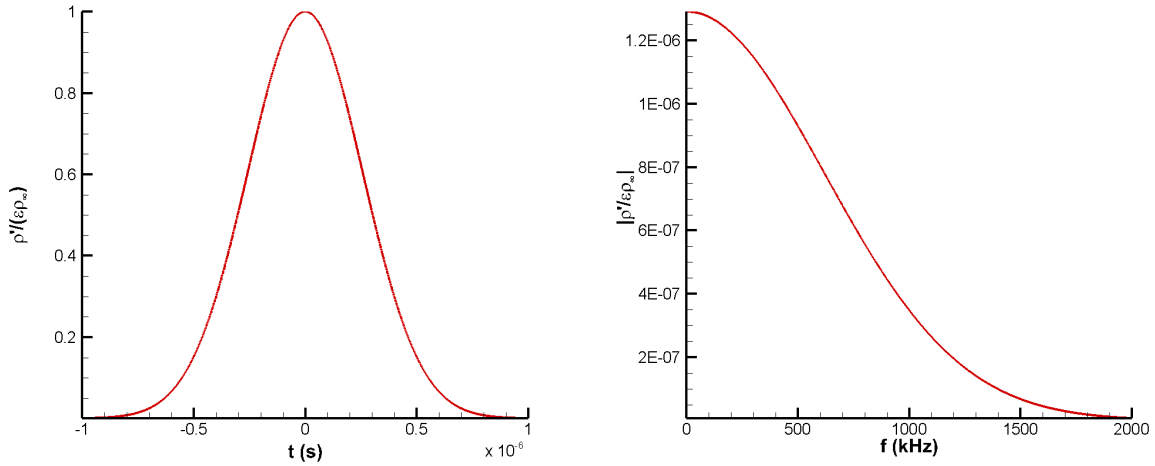

(a) (b)

Figure 2. Shape of freestream pulse for parameters specified in Table 2 in terms of normalized density perturbations ($\rho'/(\epsilon\rho_\infty)$). (a) Amplitude, in time domain. (b) Single-sided amplitude spectrum, in frequency domain

V. Steady DNS Results

The pressure, temperature, and species mass fractions along the stagnation line at the nose are shown in Figure 3. Between the two gas models, there are minimal discrepancies in pressure but significant discrepancies in temperature. That is, the real-gas T-R temperature is significantly lower compared to the frozen gas T-R temperature over most of the stagnation line. This result can be attributed to a combination of thermal nonequilibrium (TNE) and chemical nonequilibrium (CNE) effects. First, there is an energy exchange between the translation-rotation and vibration modes where if $T > T_v$, energy is transferred away from the T-R mode to the vibration mode. In this way, the vibration mode acts as an energy sink for the T-R mode.[8] Second, the dissociation of N_2 and O_2 (evidenced by the reduction in mass fractions of N_2 and O_2 in Figure 3) also acts as an energy sink for the T-R mode, since they are endothermic reactions. This reduction in T-R temperature causes the shock height to be smaller in the real-gas case, as seen in Figure 4. Specifically, the frozen shock height at the stagnation line (the standoff distance) is 0.152 mm, whereas the real-gas standoff distance is only 0.132 mm.

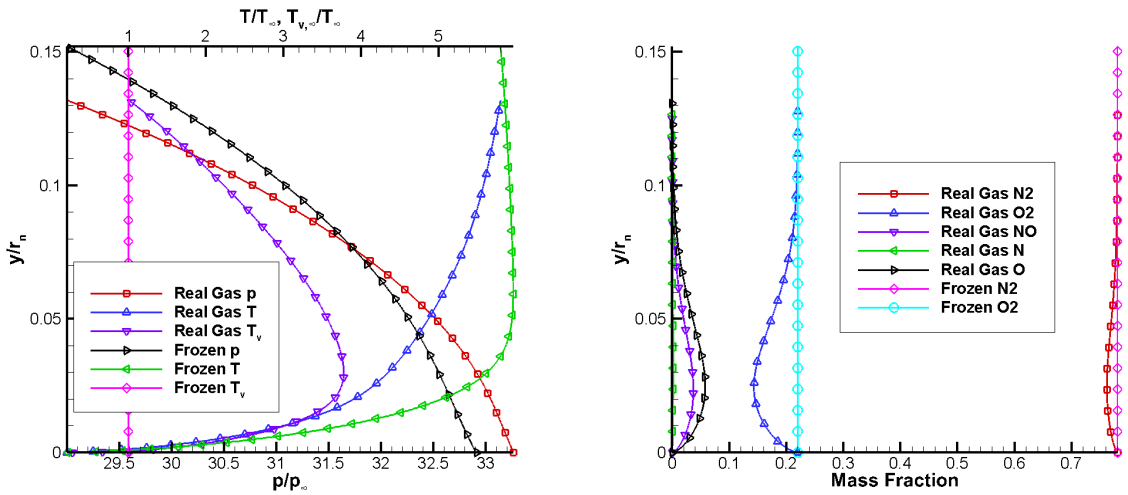

(a) (b)

Figure 3. Comparison of wall-normal profiles of select variables along stagnation line. (a) Nondimensional pressure and temperatures. (b) Species mass fractions. In this case y/r_n is the wall-normal distance where the maximum value corresponds to the shock height at the stagnation line.

The trends seen at the stagnation line continue throughout the nose region (see Figure 5). Again, pressures are similar between the real-gas and frozen cases. On the other hand, the T-R temperature shows significant discrepancies. In the real-gas case, the higher temperatures near the stagnation line decay faster moving downstream. This is again due to the nonequilibrium effects mentioned before.

Figure 6 shows the contours of T/T_v and the mass fraction of O throughout the nose region. Clearly, the ratio T/T_V does not change much moving downstream, which is an early indication that TNE effects persist downstream. Looking at Figure 3, O has the highest mass fractions (about 5.7%) out of the additional species (NO, N, O), indicating that the dissociation of O_2 is the predominant chemical reaction in the flowfield. As such, the mass fraction of O can be used as an indicator of CNE effects. However, Figure 6 shows that the mass fraction of O has decreased to only 1.7% or less by the end of the domain. Therefore, CNE effects decay very quickly in comparison to TNE effects.

Figures 7 and 8 show the boundary-layer profiles of various quantities further downstream, at $s/r_n = 50$ and $s/r_n = 500$, respectively. From the velocity profiles, it can be seen that the real-gas boundary layer is slightly more thin compared to the frozen gas. The temperature profiles show a much larger discrepancy, with a noticeably lower peak T-R temperature in the real-gas case. Since $T > T_v$ in the real-gas case, this discrepancy can again be attributed to energy being transferred away from the T-R mode and to the vibration mode. In addition, the discrepancies in the T-R and vibration temperature profiles in the real-gas case at $s/r_n = 500$ indicate that TNE effects persist very far downstream, as originally found by Knisely and Zhong.[8] In other words, the vibrational mode has still not equilibrated with the T-R mode. On the other

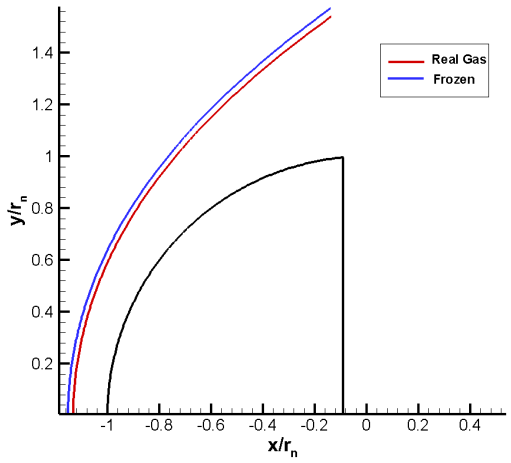

Figure 4. Comparison of shock position in nose region. Solid black lines indicate the nose shape.

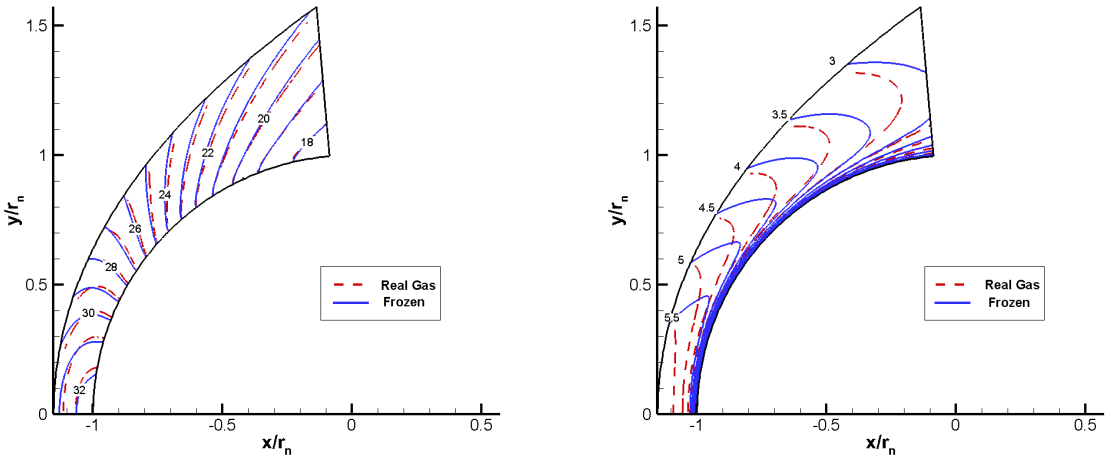

(a) (b)

Figure 5. Comparison of steady DNS contours near nose. (a) nondimensional pressure p/p_∞. (b) nondimensional T-R temperature T/T_∞

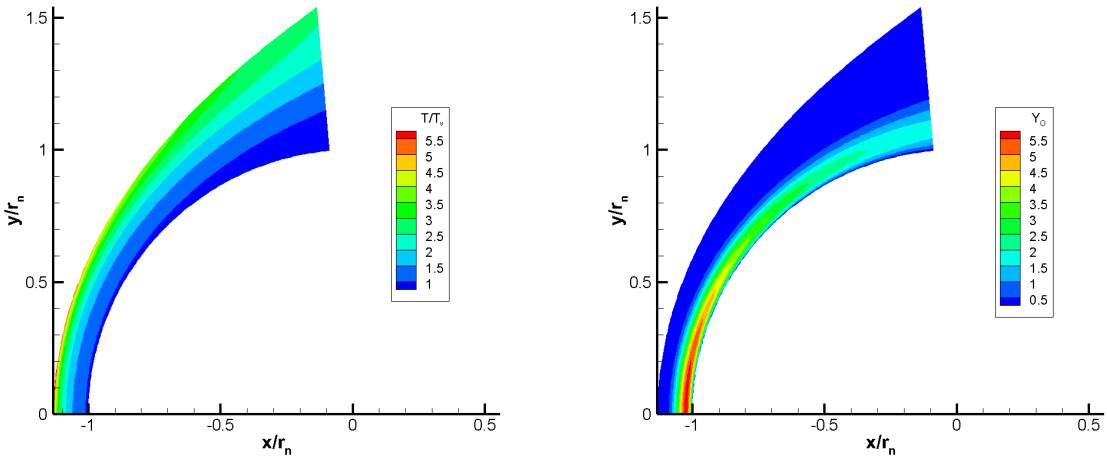

(a) (b)

Figure 6. Steady DNS contours of select variables near nose for real-gas case. (a) T/T_v, (b) O mass fraction

hand, Figure 7 shows that CNE (indicated by the mass fractions of NO, N, and O) is effectively nonexistent at $s/r_n = 50$.

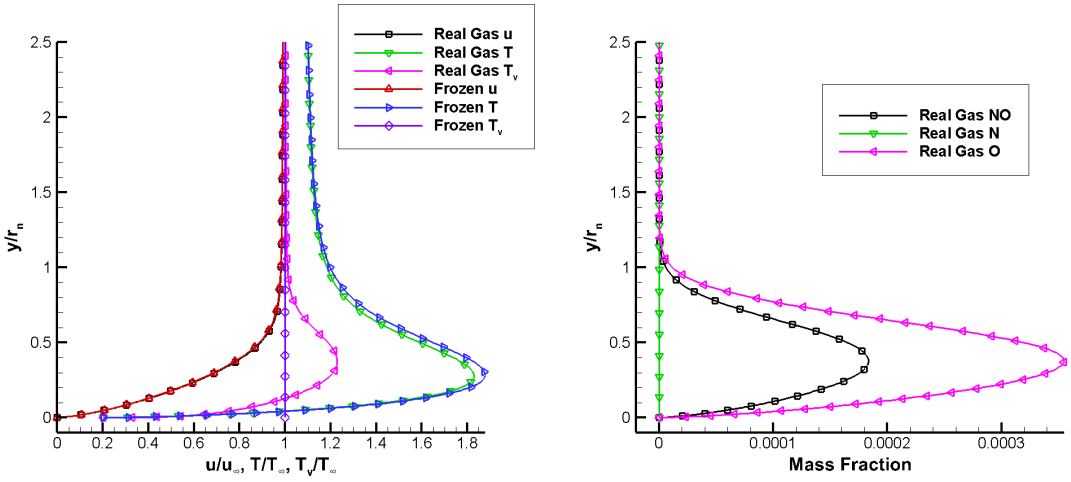

(a) (b)

Figure 7. Steady DNS boundary-layer profiles at $s/r_n = 50$ for real-gas and frozen gas models. (a) u/u_∞, T/T_∞, and T_v/T_∞. (b) Mass fraction of NO, N, and O

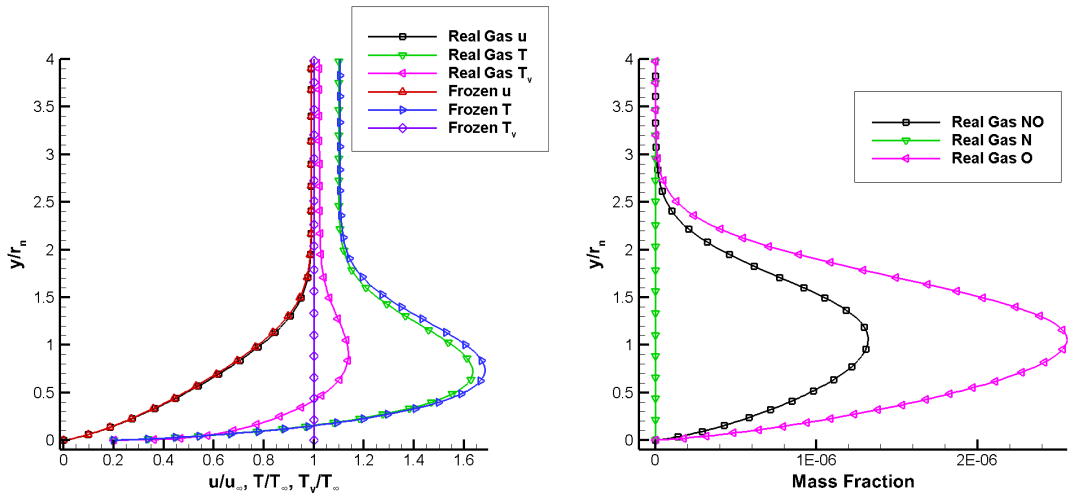

Figure 8. Steady DNS boundary-layer profiles at $s/r_n = 500$ for real-gas and frozen gas models. (a) u/u_∞, T/T_∞, and T_v/T_∞. (b) Mass fraction of NO, N, and O

VI. LST Results

In order to perform stability analysis of the boundary layer, wall-normal profiles of the flowfield are extracted from steady DNS and used as the baseflow for LST. The stability of the boundary-layer is better understood by following the streamwise evolution of the discrete modes for a fixed frequency. The streamwise evolution of the phase speed and growth rate of the relevant discrete modes at $f = 600$ kHz are presented in Figure 9. Here the phase speed c_r is normalized by the freestream velocity instead of the boundary layer edge velocity so that LST and unsteady DNS results can be compared readily. Mode F1 originates in the fast acoustic spectrum ($c_r/u_\infty \sim 1 + 1/M_\infty$) upstream, and generally decreases in phase speed moving downstream. Mode S originates in the slow acoustic spectrum ($c_r/u_\infty \sim 1 - 1/M_\infty$) upstream and generally increases in phase speed moving downstream. Mode F1 and mode S eventually reach the same phase speed at some point downstream, becoming synchronized. As a result, mode F1 is destabilized and begins to undergo eigenmode growth. This destabilization of either mode F1 or mode S due to their synchronization with each other is what is referred to in the literature as the second mode instability, although in many cases the unstable mode is mode S, rather than mode F1. Downstream of the peak growth rate location, the phase speed of mode F1 falls below that of the slow acoustic spectrum. At this point, mode F1 propagates supersonically upstream relative to the meanflow and behaves more like a continuous mode with oscillatory eigenfunctions towards the freestream.[29,35] Simultaneously, a new, stable discrete mode is generated. To distinguish between these two modes, Fedorov and Tumin[36] refer to the original mode as mode F1$^+$ and the new mode as mode F1$^-$. When mode F1$^+$ becomes stable again, it coalesces into the continuous spectrum and is no longer resolved by the LST solver. Since mode F1/F1$^+$ is the unstable mode here, the usage of the term "second mode" will hereafter refer to mode F1/F1$^+$.

Comparing the two gas models, the phase speed is initially similar but diverges downstream, with the frozen phase speed decreasing more rapidly. However, the qualitative behavior of the phase speed curve remains similar. Looking at the growth rate curves, both branch I and branch II neutral points are shifted further downstream in the real-gas case, although the branch II neutral point is shifted by a larger amount. Therefore, the overall length of the unstable second mode region is increased. It should be noted, however, that the lengthening of the second mode region is more exaggerated than for higher frequencies because of the unstable supersonic mode, which has been found to be particularly sensitive to real-gas effects.[8] In addition, the real-gas peak growth rate is larger than in the frozen case. The combination of these two factors means that the second mode will attain larger amplitudes by the time it becomes stable again. In other words, real-gas effects are overall destabilizing to the second mode. Knisely and Zhong[8] have shown that this destabilization is primarily due to TNE effects rather than CNE effects, since CNE effects subside well before the unstable second mode region (see Figure 7). They also found that TNE effects were essentially

frozen in the perturbation timescale, which means that the destabilization is due to a modification of the meanflow rather than any direct effects on the perturbation quantities themselves. However, the real-gas effects on stability seen here may not translate to receptivity, since most of the receptivity process occurs upstream, where both CNE and TNE effects are considerably stronger.

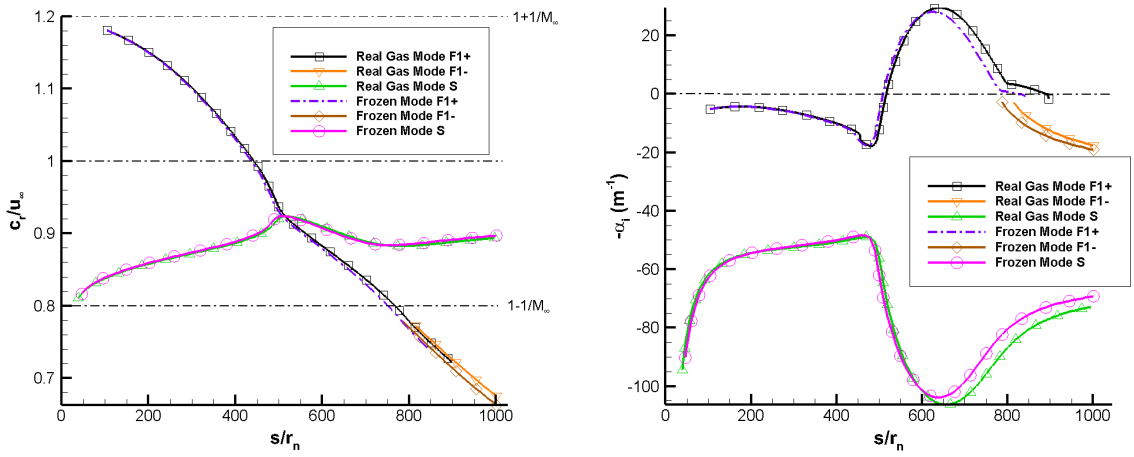

(a) (b)

Figure 9. Comparison of LST (a) phase speed and (b) growth rate for relevant boundary-layer modes vs. streamwise distance at f = 600 kHz.

By repeating the streamwise marching process for a number of frequencies, it is possible to obtain a two-dimensional neutral stability map of the second mode, which is presented in Figure 10. The broadening of the branch II neutral curve at lower frequencies is due to the unstable supersonic mode, as was shown in Figure 9. Here the supersonic mode exists only below a particular frequency, and lowering the frequency beyond this point increases the length of the supersonic mode region. It should be noted that in certain cases (particularly for the supersonic mode), the LST solver encountered convergence problems near the branch II neutral point. In such cases, the location of the branch II neutral point was simply taken as the first point at which the growth rate becomes negative again. Therefore, the neutral curves are shown for the purpose of qualitative comparison only. From Figure 10 it can be seen that real-gas effects shift both branch I and branch II neutral points further downstream. As Knisely and Zhong[8] have found, the supersonic mode is much more sensitive to real-gas effects, as evidenced by the substantially larger supersonic mode region. The supersonic mode also begins to occur at higher frequencies in the real-gas case, which means a larger range of frequencies undergo additional amplification from the supersonic mode.

To determine whether real-gas effects are stabilizing or destabilizing to second-mode growth, it is necessary to compare second-mode amplification ratios between the two gas models. Second-mode amplification ratios can be obtained by integrating the growth rate of the second mode as follows,

$$e^{N(s,f)} = \frac{A(s,f)}{A_0(f)} = -\exp\left[\int_{s_0(f)}^{s} \alpha_i(s,f)ds\right] \tag{20}$$

where for a given frequency, $A(s,f)$ is the disturbance amplitude at some location downstream of the branch I point, $A_0(f)$ is the amplitude at the branch I point (the initial amplitude), $s_0(f)$ is the location of the branch I point and N is the N-factor used in the semi-empirical e^N method of transition prediction. Note that in-flight transition N-factors are typically between 5 and 10, whereas ground test N-factors can be considerably lower. By plotting the N-factor at various streamwise distances for all unstable frequencies, it is possible to identify which frequency is most likely to cause transition. However, when comparing the N-factors of two different cases, it is more instructive to look at the largest N-factor attained out of all frequencies at some streamwise distance. The locus of these points is called the N-factor envelope, and is presented in Figure 11. At the end of the domain the real-gas N-factor is around 7.1 whereas the frozen N-factor is only around 6.4. This roughly corresponds to an 11% increase in maximum N-factor. This result

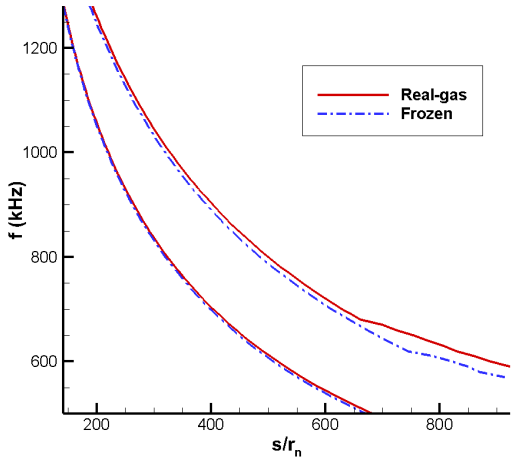

Figure 10. Comparison of LST-derived second-mode neutral curves. The curves on the left-hand side are the branch I neutral curves, where the second mode initially becomes destabilized. The curves on the right-hand side are the branch II neutral curves, where it becomes stable again.

confirms that real-gas effects (mostly TNE effects) are destabilizing to second-mode growth. However, it should be cautioned that these results only describe amplitude ratios, and not amplitudes themselves. The amplitude of the second mode at any point is also dependent on its initial amplitude, which is determined by the receptivity process. It is certainly possible that if $A_0(f)$ is small enough, the amplitude of the second mode could be smaller in the real-gas case, even though real-gas effects are predicted to be destabilizing to second mode growth. In such a scenario, predicted transition locations would move downstream if real-gas effects are considered. This highlights the importance of distinguishing between receptivity and stability for effective transition prediction.

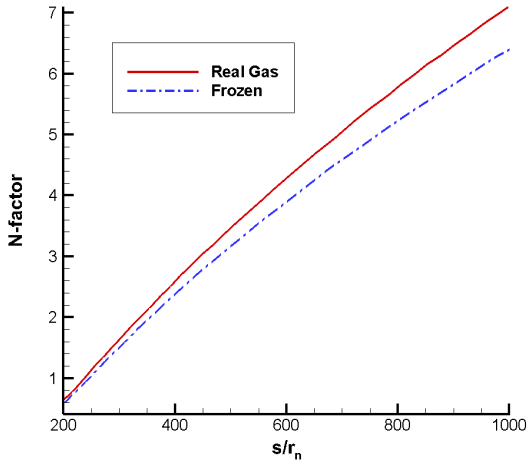

Figure 11. Comparison of LST N-factor envelope

VII. Unsteady DNS Results

A. Fast Acoustic Pulse

Upon interacting with the shock, the freestream fast acoustic pulse transmits and generates waves of all four types (fast acoustic, slow acoustic, entropy and vorticity) behind the shock.[37] Therefore, the disturbance behind the shock contains waves of all types, even if the original freestream disturbance does not. The relative magnitude of each of these wave types, which is determined by the characteristics of the flowfield in the shock layer, then govern the receptivity of the boundary-layer modes. To show how this disturbance evolves as it propagates downstream, Figure 12 shows the time trace of the wall pressure perturbation at various streamwise locations resulting from the freestream fast acoustic pulse in the real-gas case. As the disturbance propagates downstream, it excites the boundary-layer modes. The second mode then undergoes amplification. This amplification is evidenced by the distinct shape that appears in the disturbance at $s/r_n = 531$. The pressure perturbation contours of the disturbance in the second-mode growth region (near $s/r_n = 500$) can be seen in Figure 13. The beam-like shape is the freestream disturbance (which has entered the shock layer) that continues to propagate downstream. The oscillations at the wall behind this beam indicate the second mode.

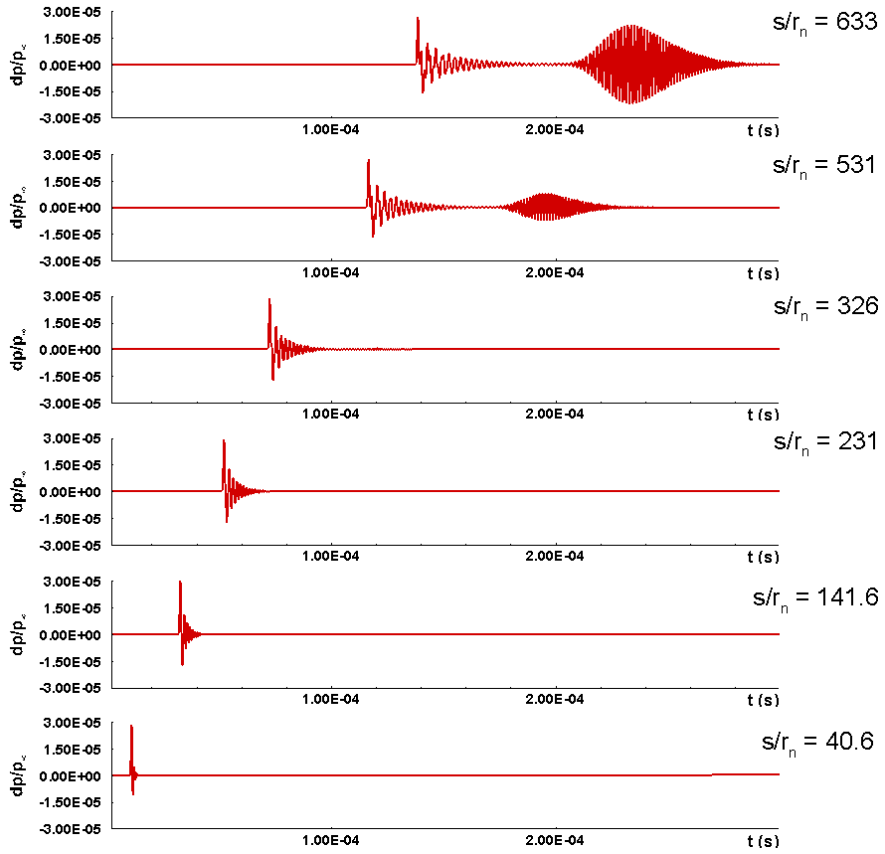

Figure 12. Time-trace of the wall pressure perturbation resulting from the fast acoustic pulse at various streamwise distances. (real-gas, fast acoustic)

The evolution of the disturbance is better understood by looking at its individual frequency components. To obtain these frequency components, FFT is applied to the time history of the wall pressure perturbation at each streamwise location. For a given frequency, the amplitude (denoted by $|\Delta p|$) and phase angle (denoted by ψ) can be obtained directly from the FFT output. The growth rate, streamwise wave number and phase speed at that frequency can then be computed using the following relations:

$$-\alpha_i(f) = \frac{1}{|\Delta p(f)|}\frac{d|\Delta p(f)|}{ds} \tag{21}$$

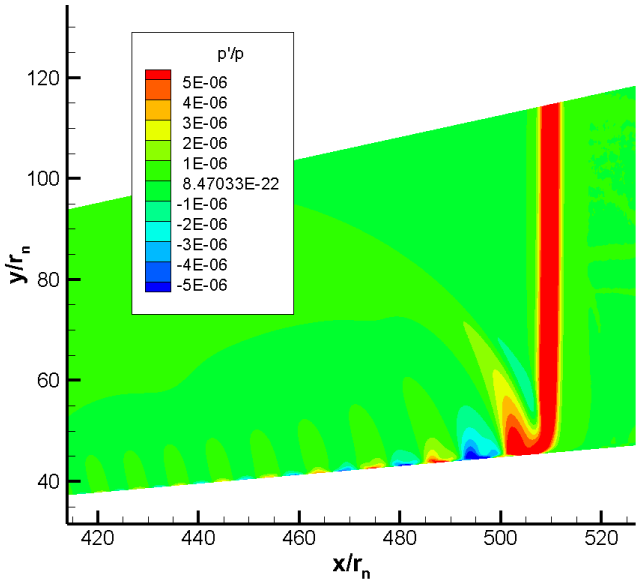

Figure 13. Snapshot of unsteady pressure perturbation contours resulting from the fast acoustic pulse. (real gas, near $x/R_n = 500$). The disturbance is propagating from the left to the right.

$$\alpha_r(f) = \frac{d\psi(f)}{ds} \tag{22}$$

$$c_r(f) = \frac{2\pi f}{\alpha_r(f)} \tag{23}$$

The disturbance frequencies that undergo the largest amplification can be identified by normalizing the amplitude spectrum of the disturbance by the amplitude spectrum of the freestream disturbance. Following the work of Huang,[30] the normalized amplitude is computed using the following expression:

$$\text{Normalized amplitude} = \frac{|p'(f)/p_\infty|}{|\rho'_\infty(f)/\rho_\infty|} \tag{24}$$

The wall pressure perturbation (in terms of the normalized amplitude) at various frequencies resulting from the fast acoustic pulse is presented in Figure 14. It should be noted that all the frequencies shown follow the same general streamwise behavior, although the lower frequencies undergo slower changes in the streamwise direction. The leading-edge receptivity region is marked by an initial sharp decrease in amplitude and then a subsequent increase, leading to a noticeable peak ($s/r_n \sim 120$ for $f = 750$ kHz). From Figure 15, it can be deduced that this amplification is due to the synchronization between the newly-generated mode F1 and the fast acoustic waves in the disturbance, since the DNS phase speed for $f = 750$ kHz in this region is near that of the fast acoustic spectrum. Also, the qualitative similarities in phase speeds and growth rates between the two gas models suggest that the fundamental mechanism of receptivity described above is essentially unchanged by real-gas effects. Moving downstream, the wall pressure perturbations then decrease in amplitude. This is because as the phase speed of mode F1 decreases, it is no longer synchronized with the fast acoustic waves. This attenuation is accompanied by strong oscillations in amplitude, which arise due to a modulation effect from the phase speed difference between mode F1 and the fast acoustic waves.[38]

The disturbance then enters the second-mode unstable region, as indicated by the large increase in amplitude downstream. As the LST results predict, higher frequencies begin second-mode growth earlier. Near the branch I point ($s/r_n \sim 350$ for $f = 750$ kHz), the amplitude of the real-gas disturbance is slightly smaller compared to the frozen disturbance. That is, if receptivity coefficients were obtained using the overall disturbance amplitude at branch I, they would indicate a weaker receptivity response in the real-gas case. However, because the overall disturbance contains multiple competing modes, this result may not

be indicative of the receptivity of the second mode itself. To definitively confirm whether real-gas effects enhance or weaken receptivity for the second mode *only*, it is necessary to isolate the amplitude of the second mode at the branch I neutral point from the overall disturbance. While it is possible to accomplish this very accurately through biorthogonal decomposition,[39] this method has not yet been extended to real-gas flows. Instead, a simpler, more approximate method from Huang and Zhong[40] will be used. This method is described in more detail later. Figure 15 shows that the phase speed oscillates about the fast acoustic spectrum near the synchronization point. Unfortunately, these oscillations make it difficult to track the DNS growth rates and phase speeds in this region. Regardless, as the disturbance approaches the peak growth rate location from LST, the DNS phase speed appears to oscillate about the LST phase speed, suggesting that the second mode has become dominant within the overall disturbance. Comparing the two gas models, it is clear that the real-gas disturbance reaches a higher peak amplitude than the frozen disturbance, with lower frequencies showing a larger difference. This result agrees with the results of Ma and Zhong,[9,10] who found that the peak amplitude of second-mode was larger for both fast and slow acoustic waves, although they did not obtain second-mode receptivity coefficients. Note that the logarithmic scale of the amplitude plots in Figure 14 makes these differences appear smaller than they really are. In reality, the peak normalized amplitude at $f = 750$ kHz is around 34 for the real gas while it is only around 25 for the frozen gas, which corresponds to a 36% increase in amplitude.

In order to determine whether real-gas effects enhance or weaken receptivity for the second mode, it is necessary to determine the second-mode receptivity coefficient, or the amplitude of the second mode at the branch I neutral point. However, because the boundary-layer disturbance in the unsteady DNS is multimodal in nature, the unsteady DNS disturbance amplitudes may not reflect the amplitude of the second mode itself. Therefore, the amplitude of the second mode must somehow be isolated from the amplitude of the overall disturbance. As mentioned before, the method described by Huang and Zhong[40] is used to accomplish this. Rearranging Equation 20, we get

$$A_0(f) = \frac{A(s,f)}{e^{N(s,f)}} \tag{25}$$

This equation tells us that the initial amplitude of the second mode can be obtained by dividing its amplitude at some sampling location (within the second-mode unstable region) by the corresponding amplification ratio (e^N) at that location. Therefore, the second-mode receptivity coefficient can be estimated from unsteady DNS results by dividing the DNS disturbance amplitude at some location by the LST amplification ratio at that location, as in the following equation:

$$C_{rec}(f) = A_0(f) \approx \frac{1}{e^N} \frac{|p'(f)/p_\infty|}{|\rho'_\infty(f)/\rho_\infty|}\bigg|_s \tag{26}$$

In order to obtain a reasonable estimate, the sampling location much be chosen carefully. The second mode should be dominant at this sampling location so that the DNS disturbance amplitude in the above equation is approximately equal to the amplitude of the second mode. Naturally, it can be assumed that the second mode is most dominant where the disturbance attains the largest amplitudes during second-mode growth. Therefore, the sampling location is chosen to be the streamwise location (within the second-mode unstable region) at which a given frequency attains its maximum amplitude.

Figure 16 shows the estimated second-mode receptivity spectra for the fast acoustic pulse, obtained using the method mentioned above. Note that receptivity coefficients for frequencies below $f = 700$ kHz were not considered reliable, since they had not reached their peak amplitudes within the domain considered. Therefore, these frequencies are not shown in this figure. Continuation of unsteady DNS further downstream will be required to obtain receptivity coefficients for these lower frequencies. Overall, it is clear that the real-gas receptivity coefficients are smaller compared to the frozen gas. That is, real-gas effects weaken receptivity, since the initial amplitude of the second mode is smaller. This indicates that real-gas effects can have competing impacts on receptivity versus stability for the second mode. While real-gas effects lead to smaller second-mode receptivity coefficients, they also destabilize second-mode growth, ultimately leading to larger maximum amplitudes. It is possible that the weaker receptivity seen in the real-gas case is actually due to energy transfer from the T-R mode to the vibration mode, which reduces boundary-layer T-R temperatures as seen in Figures 7 and 8. This possible explanation is motivated by the results of Kara *et al.*,[41] who found that wall cooling (which also causes lower boundary-layer T-R temperatures) can lead to smaller receptivity coefficients for the first mode for slow acoustic disturbances. However, further analysis is required to confirm this effect for the current study.

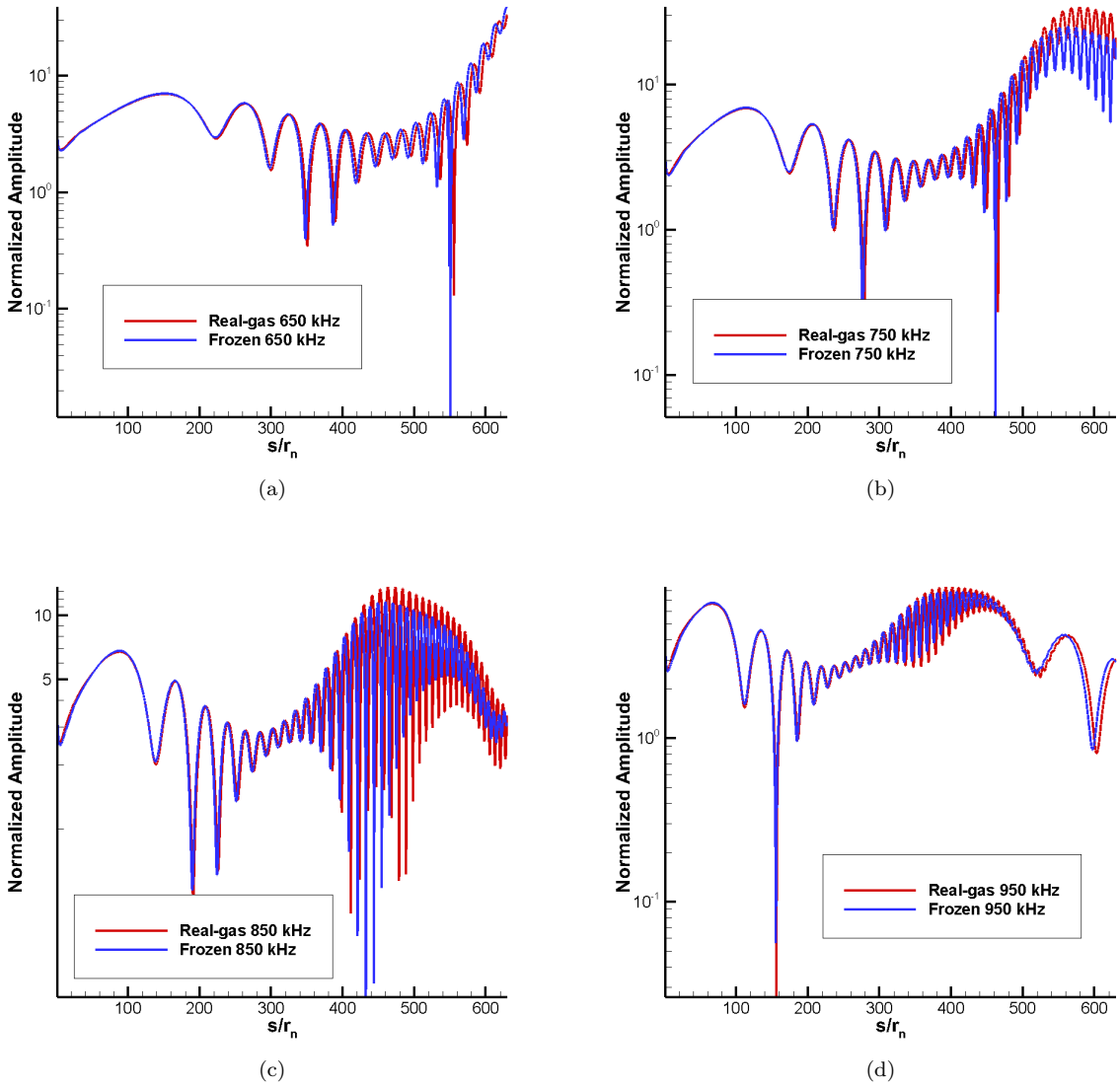

Figure 14. Normalized amplitude vs. streamwise distance for various frequencies (fast acoustic pulse)

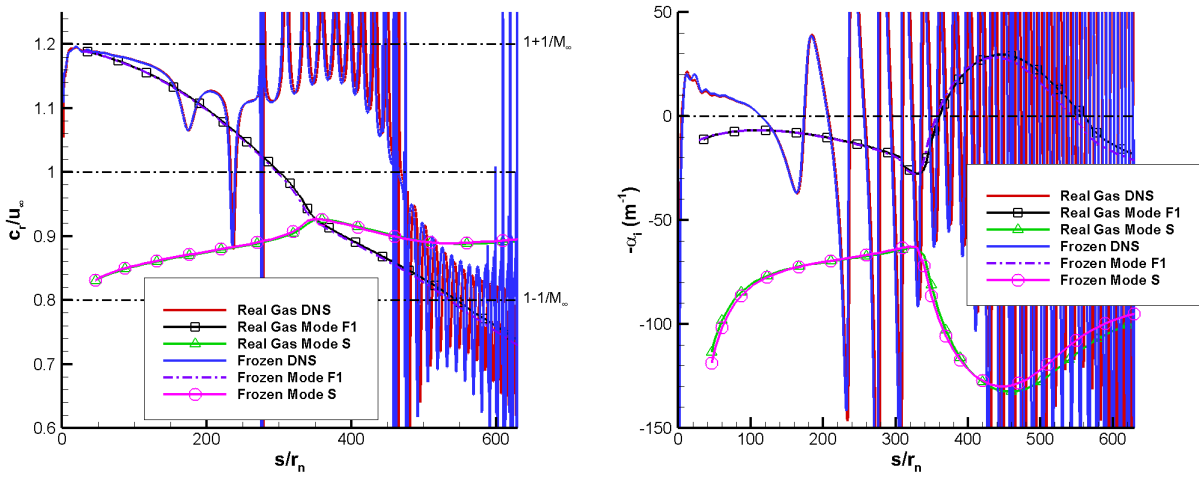

(a) (b)

Figure 15. DNS to LST comparison of (a) phase speed and (b) growth rate (fast acoustic pulse, $f = 750$ kHz)

The receptivity coefficient spectra also seem to suggest that higher frequencies are more receptive than lower frequencies. However, it is unclear whether this behavior is physical. Higher frequencies in general have stronger oscillations in the second mode region relative to their amplitude. Therefore, receptivity coefficients obtained using maximum amplitudes (as is the case here) could be overpredicted considerably. This presents a limitation to the receptivity coefficient estimation methodology used in this study when considering disturbances with strong oscillations in their amplitude. One possible solution would be to somehow filter out the oscillations before computing receptivity coefficients. Regardless, this limitation is not expected to change the comparisons between the real-gas and frozen cases, as both cases show similar oscillations.

It should also be noted that the receptivity coefficient spectra seem to have small jumps in amplitude between certain frequency bands. This is likely due to the fact that the N-factors used to obtain the receptivity coefficients are evaluated at the location of maximum amplitude for each frequency in the unsteady DNS. Because the unsteady DNS amplitudes can be highly oscillatory due to forcing, the location of maximum amplitude can become highly sensitive, leading to the jumps in the receptivity coefficient spectra. In any case, these jumps are likely insignificant, since they are much smaller in amplitude than the difference between the frozen and real-gas receptivity coefficient spectra.

B. Slow Acoustic Pulse

The wall pressure perturbation at various frequencies resulting from the slow acoustic pulse is presented in Figure 17. The qualitative behavior of the boundary-layer disturbance is similar to that of the fast acoustic pulse. However, the amplitudes are much smaller, indicating that the slow acoustic pulse is far less efficient at exciting the boundary-layer modes compared to the fast acoustic pulse. Like the fast acoustic case, the wall pressure perturbations still briefly increase in amplitude far upstream of the second-mode region. This amplification is due to the synchronization of mode S with slow acoustic waves. This can be confirmed by looking at Figure 18, which shows that the phase speed in this region oscillates about the slow acoustic spectrum. However, slow acoustic waves can only interact with the stable mode S, and not with the unstable mode F1. Therefore, the second mode amplitudes are largely determined by the energy exchange between mode S and mode F1 at their synchronization point further downstream.[34] Moving downstream, the disturbance is attenuated again because mode S and the forcing slow acoustic waves are no longer synchronized. However, immediately before the disturbance reaches the second-mode instability region, there appears to be another small peak in amplitude. Further analysis is required to determine the cause.

The disturbance then enters the second-mode unstable region, as indicated by the large increase in

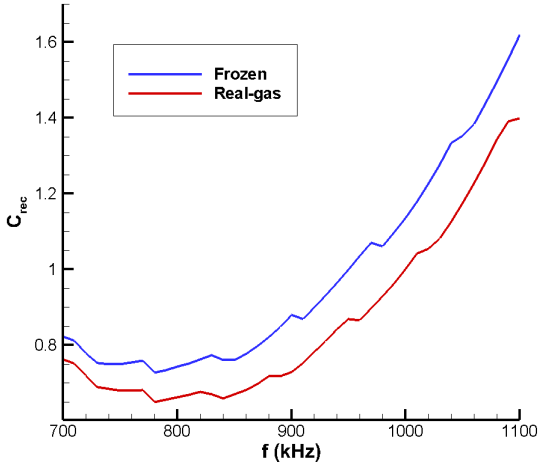

Figure 16. Second-mode receptivity coefficient spectra (fast acoustic pulse)

amplitude downstream. Again, it can be seen that higher frequencies undergo second-mode growth earlier. Near the branch I point ($s/r_n \sim 350$ for $f = 750$ kHz), the amplitude of the real-gas disturbance is smaller compared to the frozen disturbance. Figure 18 shows that both the peak growth rate and second-mode unstable region are larger in DNS compared to LST. This discrepancy, which was also noted by Knisely and Zhong,[8,29,35] may be due to nonparallel and multimodal effects that are neglected in LST. However, the growth rates and second-mode unstable regions for the real-gas case are overall larger compared to the frozen gas case, in agreement with LST predictions. In other words, real-gas effects are confirmed to be destabilizing to second mode growth. It is also clear that by the time the disturbance attains its maximum growth rate, the second mode has become dominant within the overall disturbance, as evidenced by the alignment of the DNS phase speed with the LST phase speed for mode F1. Like in the fast acoustic case, the real-gas disturbance reaches a higher peak amplitude after second-mode growth.

Figure 19 shows the second-mode receptivity coefficients for the slow acoustic pulse. The receptivity coefficients are an order of magnitude lower for the slow acoustic pulse compared to the fast acoustic pulse, in agreement with the behavior of the overall disturbance amplitudes in the receptivity region. In addition, higher frequencies seem to be more receptive. Unlike the fast acoustic case, the oscillations in amplitude are relatively weak, suggesting that this frequency-dependent behavior is likely to be physical. Overall, it can be seen that the second-mode receptivity coefficients for the real-gas case are smaller compared to the frozen case. Again, this could be due to the reduction of T-R temperatures from TNE effects, as mentioned earlier.

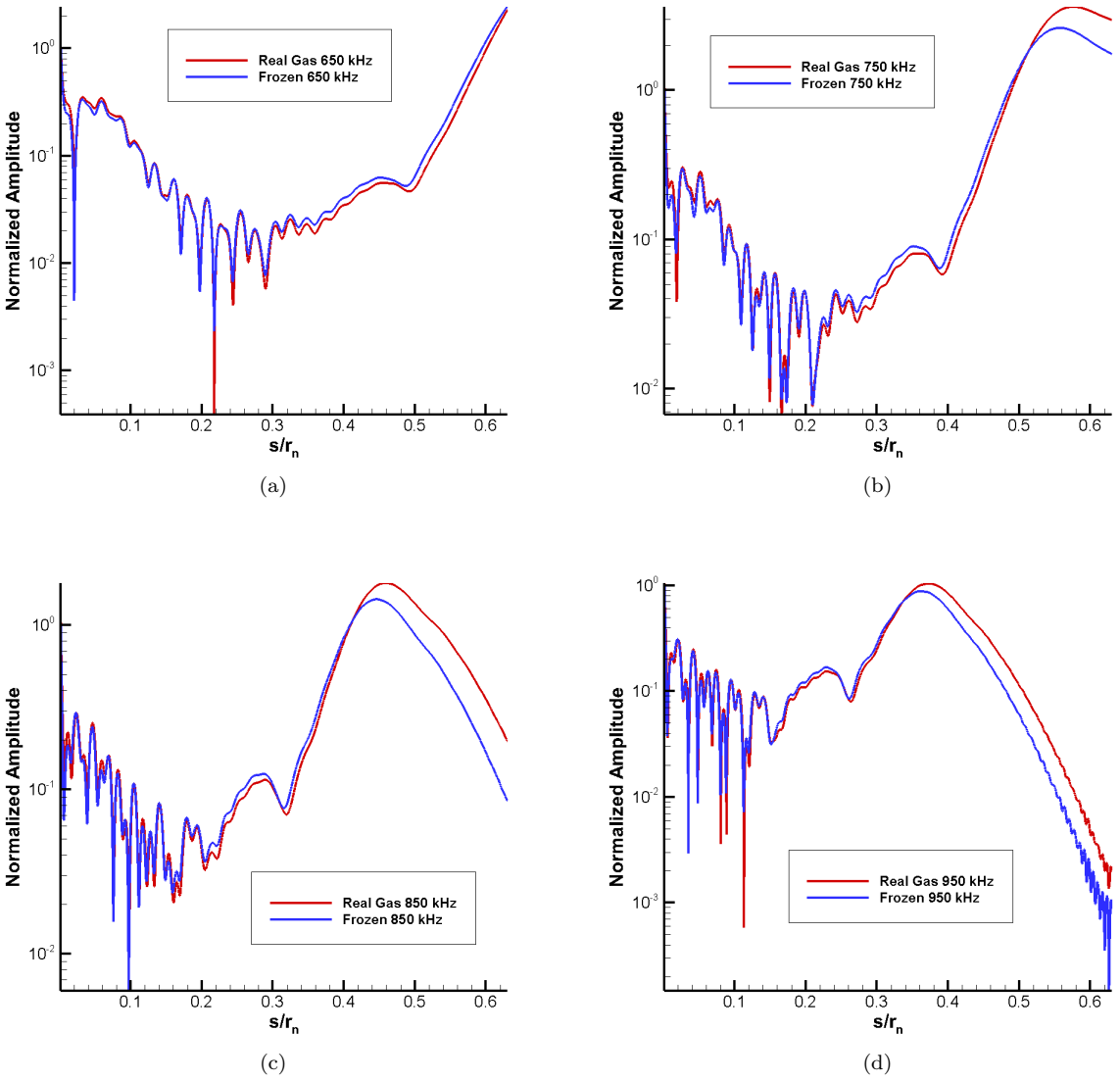

Figure 17. Normalized amplitude vs. of streamwise distance for various frequencies (slow acoustic pulse)

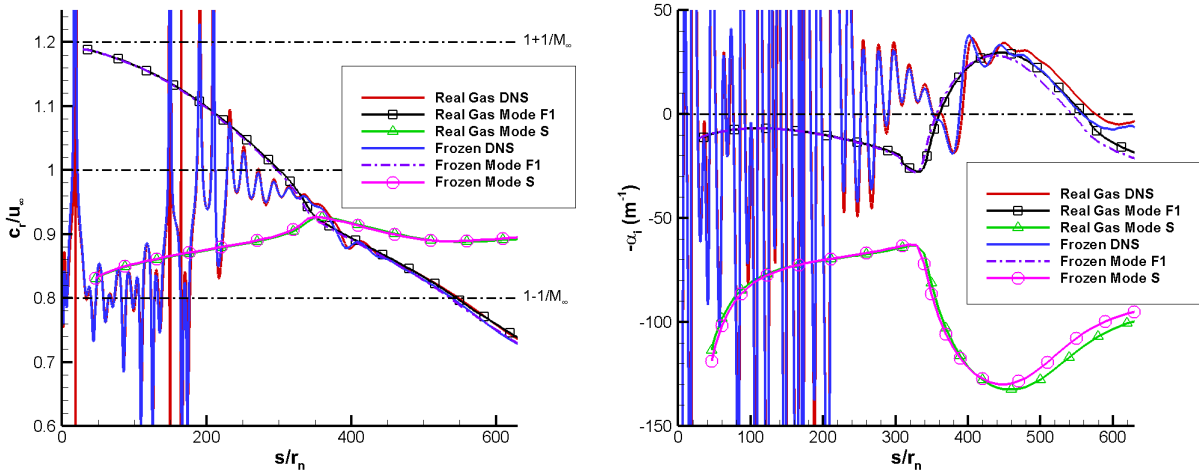

(a) (b)

Figure 18. DNS to LST comparison of (a) phase speed and (b) growth rate (slow acoustic pulse, $f = 750$ kHz)

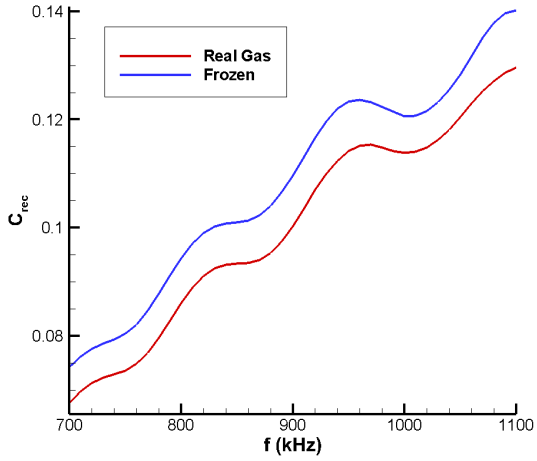

Figure 19. Second-mode receptivity coefficient spectra (slow acoustic pulse)

VIII. Conclusion and Future Work

Real-gas effects on boundary-layer receptivity to freestream disturbances for a Mach 5 blunt cone flow were investigated using a combined LST and DNS approach. To parametrize real-gas effects, two cases with different gas models were considered for the same freestream conditions and geometry. The first case uses a full 5-species thermochemical nonequilibrium gas model, whereas the second case uses a frozen gas model where the species mass fractions and vibration temperature remain at their freestream values.

The steady DNS results indicated that in the real-gas case, there are moderate CNE effects (like the dissociation and recombination of species) near the nose of the cone. However, the amount of CNE subsides quickly moving downstream. In contrast, TNE effects (like translation-vibration energy transfer) persist very far downstream. This result indicates that for this flow configuration, CNE effects have little impact on second-mode growth, which begins far downstream of the leading edge.

LST results indicated that real-gas effects, specifically TNE effects, are destabilizing to the second mode. Compared to the frozen gas case, the real-gas case featured an extended second-mode growth region and larger growth rates. This combined effect means that in the real-gas case the N-factor envelope is about 11% larger by the end of the domain ($s/r_n = 1000$). That is, given the same initial amplitude, the real-gas second mode will attain larger amplitudes before becoming stable again.

Next, the receptivity of the boundary layer to freestream fast acoustic and slow acoustic pulses was simulated using unsteady DNS. The resulting disturbance was then analyzed using FFT. The fast acoustic pulse was found to generate much stronger disturbances than the slow acoustic pulse. For both pulses, it was found that the real-gas boundary-layer disturbance attains much larger amplitudes after second-mode growth, implying that real-gas effects are ultimately destabilizing. However, the receptivity coefficients of the second mode were found to be smaller in the real-gas case compared to the frozen gas case. This result suggests that real-gas effects have competing impacts on second-mode receptivity vs. second-mode growth. While real-gas effects lead to smaller initial second-mode amplitudes, the subsequent increase in second-mode growth rates ultimately leads to larger second-mode amplitudes.

The results of this study show that real-gas effects on hypersonic boundary-layer transition should not be oversimplified. It was found that real-gas effects can have different impacts on receptivity versus stability. Therefore, it is certainly possible that even if real-gas effects are found to be stabilizing to second-mode growth in a particular flow configuration, stronger second-mode receptivity can cause transition to occur earlier. Of course, the opposite scenario could also be possible in a different flow configuration.

Lastly, it should be emphasized that the current study is still a work-in-progress, and that the results presented above may require further refinement and analysis before completion. The combination of a low wall-to-freestream temperature ratio and high second-mode frequencies makes this flow configuration especially challenging to simulate in terms of grid resolution in both the wall-normal and streamwise directions. During the course of this study, it was found that the LST and unsteady DNS results could be particularly sensitive to the wall-normal grid resolution in steady DNS. However, it is expected that the current simulations still capture the flow physics and the differences between the frozen and real-gas models quite well. In addition, the DNS and LST results have been shown to agree quite well. Therefore, the conclusions made above are not expected to change. Nevertheless, future work involves obtaining improved results using steady DNS meanflows with higher grid resolutions. In addition, the receptivity simulations for both the fast and slow acoustic pulses will be continued further downstream to obtain receptivity coefficients for lower frequencies. Finally, the exact mechanism by which real-gas effects weaken second-mode receptivity will be determined.

IX. Acknowledgments

This research was partially supported by the AFOSR, under AFOSR Grant #FA9550-19-1-0206, currently monitored by Dr. Sarah Popkin and previously by Dr. Ivett Leyva, and by Office of Naval Research (ONR) Grant #N00014-17-1-2343, first monitored by Dr. Knox Millsaps and later by Dr. Eric Marineau. Primary computational resources were provided by Extreme Science and Engineering Discovery Environment (XSEDE) through the Texas Advanced Computing Center (TACC) and San Diego Supercomputer Center (SDSC) under grant number TG-ASC090076, supported in part by the National Science Foundation. Additional computational support was provided by the Department of Defense High Performance Computing Modernization Program (DoD HPCMP) through project AFOSR40702004. The views and conclusions con-

tained herein are those of the authors and should not be interpreted as necessarily representing the official policies or endorsements, either expressed or implied, of the U.S. Air Force Office of Scientific Research, Office of Naval Research, or the U.S. Government.

References

[1]Mack, L. M., "Boundary Layer Linear Stability Theory," Tech. rep., AGARD report No. 709, 1984.

[2]Malik, M. R., "Hypersonic flight transition data analysis using parabolized stability equations with chemistry effects," *Journal of Spacecraft and Rockets*, Vol. 40, No. 3, 2003, pp. 332–344.

[3]Chang, C.-L., Vinh, H., and Malik, M., "Hypersonic Boundary-Layer Stability with Chemical Reactions using PSE," *28th AIAA Fluid Dynamics Conference, Snowmass Village, CO, U.S.A.*, 1997.

[4]Stuckert, G. and Reed, H., "Linear Disturbances in Hypersonic, Chemically Reacting Shock Layers," *AIAA Journal*, Vol. 32, No. 7, 1994, pp. 1384–1393.

[5]Johnson, H. B., Seipp, T. G., and Candler, G., "Numerical study of hypersonic reacting boundary layer transition on cones," *Physics of Fluids*, Vol. 10, No. 10, 1998, pp. 2676–2685.

[6]Hudson, M. L., Chokani, N., and Candler, G., "Linear Stability of Hypersonic Flow in Thermochemical Nonequilibrium," *AIAA Journal*, Vol. 35, No. 6, 1997, pp. 958–964.

[7]Mortensen, C., "Toward an understanding of supersonic modes in boundary-alyer transition for hypersonic flow over blunt cones," *Journal of Fluid Mechanics*, Vol. 846, 2018, pp. 789–814.

[8]Knisely, C. and Zhong, X., "Impact of Vibrational Nonequilibrium on the Supersonic Mode in Hypersonic Boundary Layers," *AIAA Journal*, Vol. 58, No. 4, 2019.

[9]Ma, Y. and Zhong, X., "Numerical Simulation of Receptivity and Stability of Nonequilibrium Reacting Hypersonic Boundary Layers," *AIAA 2001-0892*, 2001.

[10]Ma, Y. and Zhong, X., "Receptivity to Freestream Disturbances of a Mach 10 Nonequilibrium Reacting Oxygen Flow over A Flat Plate," *AIAA 2004-0256*, 2004.

[11]Parsons, N., Zhong, X., Kim, J., and Eldredge, J., "Numerical Study of Hypersonic Receptivity with Thermochemical Non-Equilibrium on a Blunt Cone," *AIAA 2010-4446*, 2010.

[12]Prakash, A., *Numerical Simulation of Receptivity to Freestream Acoustic Disturbances for Hypersonic Boundary Layer over a Blunt Body with Chemical and Thermal Nonequilibrium*, Ph.D. thesis, University of California, Los Angeles, 2011.

[13]Knisely, C. and Zhong, X., "An Investigation of Sound Radiation by Supersonic Unstable Modes in Hypersonic Boundary Layers," *AIAA 2017-4516*, 2017.

[14]Mortensen, C. H. and Zhong, X., "High-Order Shock-Fitting Method for Hypersonic Flow with Graphite Ablation and Boundary Layer Stability," *AIAA 2012-3150*, 2012.

[15]Mortensen, C. H. and Zhong, X., "Numerical Simulation of Graphite Ablation Induced Outgassing Effects on Hypersonic Boundary Layer Receptivity over a Cone Frustum," *AIAA 2013-0522*, 2013.

[16]Mortensen, C. H. and Zhong, X., "Real Gas and Surface Ablation Effects on Hypersonic Boundary Layer Instability over a Blunt Cone," *AIAA 2013-2981*, 2013.

[17]Mortensen, C. H. and Zhong, X., "Simulation of Second-Mode Instability in a Real-Gas Hypersonic Flow with Graphite Ablation," *AIAA Journal*, Vol. 52, No. 8, 2014, pp. 1632–1652.

[18]Mortensen, C. H. and Zhong, X., "Numerical Simulation of Hypersonic Boundary-Layer Instability in a Real Gas with Two-Dimensional Surface Roughness," *AIAA 2015-3077*, 2015.

[19]Mortensen, C. H., *Effects of Thermochemical Nonequilibrium on Hypersonic Boundary-Layer Instability in the Presence of Surface Ablation and Isolated Two-Dimensional Roughness*, Ph.D. thesis, University of California Los Angeles, 2015.

[20]Park, C., *Nonequilibrium Hypersonic Aerothermodynamics*, John Wiley & Sons Inc., New York, 1990.

[21]Lee, J., "Basic Governing Equations for the Flight Regimes of Aeroassisted Orbital Transfer Vehicles," *Thermal Design of Aeroassisted Orbital Transfer Vehicles*, edited by H. F. Nelson, Vol. 96, AIAA, 1985, pp. 3–53.

[22]Blottner, F., Johnson, M., and Ellis, M., "Chemically Reacting Gas Viscous Flow Program for Multi-Component Gas Mixtures," Tech. Rep. SC-RR–70-754, Sandia National Laboratories, 1971.

[23]Wilke, C., "A Viscosity Equation for Gas Mixtures," *The Journal of Chemical Physics*, Vol. 18, No. 4, 1950, pp. 517–519.

[24]Zhong, X., "High-Order Finite-Difference Schemes for Numerical Simulation of Hypersonic Boundary-Layer Transition," *Journal of Computational Physics*, Vol. 144, No. 2, 1998, pp. 662–709.

[25]Liu, Y. and Vinokur, M., "Nonequilibrium Flow Computations. I. An Analysis of Numerical Formulations of Conservation Laws," *Journal of Computational Physics*, Vol. 83, No. 2, 1989, pp. 373–397.

[26]Shu, C.-W. and Osher, S., "Efficient implementation of essentially non-oscillatory shock-capturing schemes," *Journal of Computational Physics*, Vol. 77, No. 2, 1988, pp. 439–471.

[27]Scalabrin, L., *Numerical Simulation of Weakly Ionized Flow Over Reentry Capsules*, Ph.D. thesis, University of Michigan, 2007.

[28]Knisely, C., *Supersonic Unstable Modes in Hypersonic Boundary Layers with Thermochemical Nonequilibrium Effects*, Ph.D. thesis, University of California, Los Angeles, 2018.

[29]Knisely, C. and Zhong, X., "Sound radiation by supersonic unstable modes in hypersonic blunt cone boundary layers. II. Linear stability theory." *Physics of Fluids*, Vol. 31, 2019.

[30]Huang, Y., *Numerical Study of Hypersonic Boundary-Layer Receptivity and Stability with Freestream Hotspot Perturbations*, Ph.D. thesis, University of California Los Angeles, 2016.

[31]He, S. and Zhong, X., "Hypersonic Boundary Layer Receptivity over a Blunt Cone to Freestream Pulse Disturbances," *AIAA 2020-2057*, 2020.

[32]Ma, Y. and Zhong, X., "Receptivity of a supersonic boundary layer over a flat plate. Part 1. Wave structures and interactions," *Journal of Fluid Mechanics*, Vol. 488, 2003, pp. 31–78.

[33]Ma, Y. and Zhong, X., "Receptivity of a supersonic boundary layer over a flat plate. Part 2. Receptivity to free-stream sound," *Journal of Fluid Mechanics*, Vol. 488, 2003, pp. 31–78.

[34]Ma, Y. and Zhong, X., "Receptivity of a supersonic boundary layer over a flat plate. Part 3. Effects of different types of free-stream disturbances," *Journal of Fluid Mechanics*, Vol. 488, 2003, pp. 31–78.

[35]Knisely, C. and Zhong, X., "Sound radiation by supersonic unstable modes in hypersonic blunt cone boundary layers. II. Direct numerical simulation," *Physics of Fluids*, Vol. 31, 2019.

[36]Fedorov, A. and Tumin, A., "High-speed boundary-layer instability: old terminology and a new framework," *AIAA Journal*, Vol. 49, No. 8, 2011, pp. 1647–1657.

[37]McKenzie, J. F. and Westphal, K. O., "Interaction of Linear Waves with Oblique Shock Waves," *The Physics of Fluids*, Vol. 11, No. 11, November 1968.

[38]Cerminara, A., *Boundary-Layer Receptivity and Breakdown Mechanisms for Hypersonic Flow over Blunt Leading-Edge Configurations*, Ph.D. thesis, University of Southampton, June 2017.

[39]Miselis, M., Huang, Y., and Zhong, X., "Modal Analysis of Receptivity Mechanisms for a Freestream Hot-Spot Perturbation on a Blunt Compression-Cone Boundary Layer," *AIAA 2016-3345*, 2016.

[40]Huang, Y. and Zhong, X., "Numerical Study of Hypersonic Boundary-Layer Receptivity with Freestream Hotspot Perturbations," *AIAA Journal*, Vol. 52, No. 12, December 2014.

[41]Kara, K., Balakumar, P., and Kandil, O., "Effects of Wall Cooling on Hypersonic Boundary Layer Receptivity over a Cone," *AIAA 2008-3734*, 2008.